This is a preprint, the final version is subject to change, of the American Mineralogist (MSA)
Cite as Authors (Year) Title. American Mineralogist, in press.
DOI: https://doi.org/10.2138/am-2019-6834

Revision 1: Fate of cobalt and nickel in mackinawite during diagenetic pyrite formation

Authors: Elizabeth D. Swanner[1,2], Samuel M. Webb[3], Andreas Kappler[2]

Affiliations: [1]Department of Geological & Atmospheric Sciences, Iowa State University, 2237 Osborn Dr., 253 Science Hall, Ames, IA 50011-1027; [2]Center for Applied Geoscience, University of Tübingen, Hölderlinstrasse 12, 72076 Tübingen, Germany; Stanford Synchrotron Radiation Lightsource, SLAC National Accelerator Laboratory, 2575 Sand Hill Road, MS 69, Menlo Park, CA 94025

Abstract

As iron-sulfide mineral phases are important sedimentary sinks for naturally occurring or contaminant metals, it is important to know the fate of metals during diagenetic transformation of primary sulfide minerals into more stable phases, such as pyrite (FeS_2). Furthermore, the trace metal content of pyrite has been proposed as a marine paleoredox proxy. Given the diverse low-temperature diagenetic formation pathways for pyrite, this use of pyrite requires validation. We therefore studied nickel (Ni) and cobalt (Co) incorporation into freshly-precipitated mackinawite (FeS_m), and after experimental diagenesis to pyrite (FeS_2) using S^0 as an oxidant at 65°C. Metal incorporation was quantified on bulk digests using ICP-OES or ICP-AES. Bulk mineralogy was characterized with micro-X-ray diffraction (micro-XRD), documenting transformation of mackinawite to pyrite. Epoxy mounts were made anoxically of mackinawite and pyrite grains. We used synchrotron-based micro-X-ray Fluorescence (μXRF) to map the distribution of Co and Ni, as well as to collect multiple energy maps throughout the sulfur (S) K-edge. Iron (Fe) and S K-edge micro-X-ray absorption near edge spectroscopy

(μXANES) was used to identify the oxidation state and mineralogy within the experimentally synthesized and diagenetically transformed minerals, and map end-member solid phases within the grain mounts using the multiple energy maps. Metal-free FeS_m transformed to pyrite, with residual FeS_m detectable. Cobalt- and Ni-containing FeS_m also transformed to pyrite, but with multiple techniques detecting FeS_m as well as S^0, implying less complete transformation to pyrite as compared to metal-free FeS_m. These results indicate that Co and Ni may inhibit transformation for FeS_m to pyrite, or slow it down. Cobalt concentrations in the solid diminished by 30% during pyrite transformation, indicating that pyrite Co may be a conservative tracer of seawater or porewater Co concentrations. Nickel concentrations increased several-fold after pyrite formation, suggesting that pyrite may have scavenged Ni from dissolution of primary FeS_m grains. Nickel in pyrites thus may not be a reliable proxy for seawater or porewater metal concentrations.

Keywords: mackinawite, pyrite, diagenesis, cobalt, nickel, X-ray absorption spectroscopy, X-ray Fluorescence

Introduction

Pyrite (FeS_2) is the most abundant iron sulfide mineral on the surface of the Earth (Rickard and Luther III 2007) and has formed in marine sediments (e.g. "diagenetic" pyrite) for at least 3.5 billion years (Gy) (Shen et al. 2001). The presence of pyrite, as well as its isotopic and elemental composition, has been applied to determining the redox conditions of the site of deposition, as well as the atmosphere and oceans. For instance, the presence of detrital pyrite in sediments > 2 Gy old was one of the early indications of

an anoxic Archean atmosphere (Holland 1984). Because of the enhanced mobilization of sulfate to the oceans from weathering of continental pyrite as oxygen appeared in the atmosphere, the presence of marine pyrite, formed either authigenically or diagenetically, tracks the timing of oxidation of the Earth and atmosphere. Pyrite Fe and S isotopes are exploited to track the magnitude of pyrite burial through time (Rouxel et al. 2005; Tostevin et al. 2014), the amount of sulfate in the oceans (Canfield and Farquhar 2009), as well as atmospheric and ocean oxygenation (Mojzsis et al. 2003; Rouxel et al. 2005; Konhauser et al. 2011; Fakhraee et al. 2018).

Increasingly, though, scientists are also looking into the trace metal inventory of sedimentary pyrite as a reflection of the trace metal contents and conditions of the overlying water column. While investigations of trace metals in bulk clastic sediments, such as shales, are useful for this purpose, these studies tend to better highlight the utility of elements that undergo extreme authigenic enrichments in sediments under certain redox conditions (Algeo and Maynard 2004; Algeo and Rowe 2012), rather than those that are specifically incorporated by pyrite. The trace metals that become incorporated into pyrite by co-precipitation can reflect either the abundance of these elements in seawater (Huerta-Diaz and Morse 1992), and the metals can be sequentially extracted from existing sulfide phases (Huerta-Diaz and Morse 1990). Such targeted extractions can be extremely useful for modern sediments where multiple sulfide minerals may be present (Scholz and Neumann 2007; e.g. Olson et al. 2017).

As sediments lithify, there is a potential for resetting of the trace metal contents by diagenesis, fluid alteration, or metamorphism. Extraction of pyrites and associated trace elements in clastic rocks is subject to limitations based on extraction efficiency, or

extraction specificity (Harrison et al. 1973). *In situ* analysis of trace metals in pyrite by methods such as laser ablation ICP-MS (e.g. Large et al. 2014; Gregory et al. 2015) or electron microprobe microanalysis (EPMA) coupled to wavelength-dispersive spectroscopy (WDS) have the utility of unambiguously assigning metal enrichments to pyrite vs. other phases (e.g. organics, detrital minerals, or authigenic precipitates such Fe- and/or Mn-oxides) (Chappaz et al. 2014). Laser ablation ICP-MS paths and quantitative elemental maps made by EPMA of individual pyrite grains, nodules, or framboids can also help to distinguish primary enrichments of trace metals from later overgrowths (Large et al. 2009; Swanner et al. 2013). Such findings are valuable to understanding pathways for economically significant trace metal enrichments (Tardani et al. 2017).

The availability of bioessential metals [e.g. nickel (Ni), cobalt (Co), copper (Cu), Mo, Zn, Se, etc.) in the Precambrian oceans is widely agreed to have controlled the origination and activity of microbial functional groups throughout Earth's history, due to the use of metals as active centers in enzymes or in organic co-factors (Anbar and Knoll 2002). While there has been an effort to infer changes in the abundance of metals in the environment through the genomic and metallomic inventory of modern organisms (Dupont et al. 2006, 2010), direct sedimentary records of metal availability are necessary for constraining the availability of metals (Robbins et al. 2016). As with modern sediments discussed above, the bulk rock inventory or trace metals in shales deposited throughout Earth's history is useful for informing general metal availability in the early oceans (e.g. Scott et al. 2008, 2012). Mineral specific metal analyses of chemical sediments, such as iron formations (Konhauser et al. 2009; Partin et al. 2013; Robbins et al. 2013; Swanner et al. 2014; Chi Fru et al. 2016), and in situ metal quantification

92 directly from diagenetic pyrite (Large et al. 2014; Swanner et al. 2014; Long et al. 2016)
93 can complement bulk analyses, and even provide direct estimates of seawater
94 concentrations of some elements (Konhauser et al. 2009). Multiple, temporally-resolved
95 metal records from several sedimentary reservoirs highlight the co-evolution of life and
96 its role in influencing ocean and atmospheric redox chemistry, in addition to its reaction
97 to it (Robbins et al. 2016).
98 Cobalt and Ni are a bioessential elements that are incorporated into iron sulfide
99 precipitates (e.g. mackinawite), unlike metals that precipitate directly with sulfide (e.g.
100 HgS) (Morse and Arakaki 1993), a result of the kinetics of exchange between water
101 ligands for sulfide (S^{2-}) (Morse and Luther III 1999). This means that the incorporation of
102 Co and Ni into mackinawite is predictable with a partition coefficient (Morse and
103 Arakaki 1993), an observation validated by the near-quantitative incorporation of these
104 elements from porewaters into sulfide minerals, including pyrite (Scholz and Neumann
105 2007; Olson et al. 2017). Changes in the marine Co reservoir through time determined
106 from pyrite, bulk black shale and iron formation Co contents are consistent, and indicate
107 that pyrite Co contents may reflect concentrations in the water column (Swanner et al.
108 2014). Nickel is expected to behave similarly in the pyrite system (Morse and Arakaki
109 1993). Using the marine sedimentary record as an indicator of marine metal reservoirs
110 presumes that diagenesis does not alter the original metal contents of these sediments.
111 However, diagenetic metal mobilization is a possibility for iron (oxy)hydroxides
112 (Frierdich et al. 2011), and loss, gain or redistribution of Co or Ni could occur as primary
113 iron sulfides (e.g. mackinawite, greigite, or the aqueous FeS cluster, FeS_{aq}) are

transformed to pyrite during low-temperature diagenesis (i.e. <80°C) or later fluid alteration.

The formation pathways of pyrite are debated, but it is generally understood that pyrite forms from an aqueous or precipitated FeS phase, such as mackinawite, greigite or an aqueous or nanoparticulate FeS cluster (e.g. FeS_{aq}) (Luther and Rickard 2005). At low temperatures (i.e. below 80°C), hydrogen sulfide (H_2S) is the product of microbial sulfate reduction at circumneutral pH (Jørgensen 1982), which can then precipitate with dissolved Fe^{2+} to form an FeS phase. The presence of S in the S^{1-} oxidation state in pyrite indicates that S in any primary FeS precipitate must be oxidized from S^{2-}, and Fe removed (or S added) to form the mineral pyrite (Goldhaber and Kaplan 1974). This has been accomplished experimentally through oxidation of FeS solids (mackinawite or greigite) with S^0 (Berner 1970; Sweeney 1972; Schoonen and Barnes 1991b), polysulfides (i.e. chains of S^0 and S^{-1}) (Rickard 1969; Hunger and Benning 2007), or H_2S (Rickard 1997; Rickard and Luther III 1997; Butler and Rickard 2000). Although the degree to which solid FeS minerals such as mackinawite actually exists in sediments has been questioned due to bias with the traditional acid-volatile sulfide (AVS) extraction (Rickard and Morse 2005), numerous studies have directly detected mackinawite (Burton et al. 2009; Morgan et al. 2012a; Kraal et al. 2013) and greigite (Keene et al. 2011) in the environment, justifying the use of these solids as precursor material. Another possible formation route is direct pyrite formation through reductive dissolution or surface reactions of Fe(III) (oxyhydr)oxide minerals with H_2S or polysulfides (Hellige et al. 2012; Peiffer et al. 2015; Wan et al. 2017). While specific mechanistic details vary, reaction of dissolved species and dissolution or recrystallization of an initial solid phase,

such as mackinawite or greigite, and subsequent nucleation of pyrite are generally invoked (Wang and Morse 1996; Rickard and Luther III 1997). Such reactions could mobilize trace metals co-precipitated or adsorbed with precursor phases.

In this study, two different pathways were used to convert freshly-precipitated mackinawite (FeS_m) containing Co and/or Ni into pyrite. The amount of metal in the FeS_m and pyrite were quantified by bulk and microscale techniques, in order to determine whether these metals are retained through diagenesis. Bulk and microscale techniques for both mineralogy and trace element quantification were coupled to give insights on the influence of these metals in promoting or inhibiting diagenetic pyrite formation.

Methods

Mineral Synthesis

Mackinawite (FeS_m) was synthesized from solutions of 0.6 M ferrous ammonium sulfate ($Fe(NH_4)_2(SO_4)_2$)and 0.6 M sodium sulfide (Na_2S)(Rickard 1997). Both solutions were made with ultrapure water (conductivity 0.052 μS) that had been boiled and cooled under an N_2 stream to make it anoxic. Sodium sulfide crystals were washed for 30 s with anoxic water in order to remove any oxidized S-species from the surface, then water was removed with a Pasteur pipette. Washed crystals were dried under an N_2 stream and stored in a N_2 atmosphere within a glass bottle with a butyl rubber stopper. Washed sodium sulfide crystals were weighed in an anoxic glovebox (100% N_2). The ferrous ammonium sulfate and sodium sulfide solutions were made in glass serum bottles and sealed with butyl rubber stoppers with an N_2 headspace. To synthesize FeS_m, equal volumes of each solution were added via N_2-purged syringes to a previously N_2-purged

and stoppered serum bottle under a slight vacuum (0.5 mbar). FeS_m precipitated immediately. For synthesis of FeS_m that contained either Ni or Co, 4.7 mg $NiCl_2 \cdot 6H_20$ or 190 mg $CoCl_2 \cdot 6H_20$ powders were weighed into serum bottles and stoppered, then flushed with N_2. This was accomplished by introducing N_2 through a long needle, which bubbled the solution, and letting the overpressure escape through a second, shorter needle. An appropriate volume of the ferrous ammonium sulfate solution was added to achieve concentrations of 500 μM Ni or 2000 μM Co when mixed with the sodium sulfide solution. These solutions were then mixed with sodium sulfide as described above.

Pyrite synthesis was attempted by two different methods. The first, oxidation of FeS_m with H_2S (Rickard 1997) (hereafter "H_2S oxidation), was attempted in order to circumvent introduction of other solid S species (e.g. elemental sulfur, S^0) that would be detected with later microanalysis. The reaction 13323-4 of Rickard (1997) was chosen (400 mg ferrous ammonium sulfate, 80°C, pH 6, -250 mV, 4 mM H_2S), as partial pyrite synthesis was reported from that reaction (80% pyrite and 20% mackinawite). Partial synthesis was desirable so that the partitioning of Co and Ni between the primary and secondary mineral could be evaluated. The anoxic solution of Ti(III)citrate and the phthalate buffer were made as described (Rickard 1997). The Na_2S solution was made as described for mackinawite synthesis, but then adjusted to pH 6 with anoxic 1N HCl. Dry FeS_m was weighed into a glass headspace vial with a small stir bar, and closed with a stopper inside the glovebox. The buffer solution, Ti(III)citrate solution, and the Na_2S solution were introduced via syringes that had been flushed with N_2. The mixture was

incubated in a sand bath at 80°C on a temperature regulated hot plate, stirring, for either 4 or 20 days. At the end of the reaction, the headspace was flushed with N_2.

The second pyrite synthesis method reacted FeS_m with orthorhombic sulfur (S_8, with sulfur in the S^0 oxidation state) (Schoonen and Barnes 1991b), hereafter "sulfur oxidation". FeS_m was synthesized as described above. Dried FeS_m (see below) was resuspended with pH 6 anoxic phthalate buffer in a stoppered serum vial. Orthorhombic sulfur was weighed, and placed into a stoppered headspace vial, then the headspace was exchanged with N_2. Inside the glovebox, the orthorhombic sulfur and a small stir bar were added to the FeS_m-buffer solution and crimped with butyl rubber stoppers. The vials were place in a sand bath at 65°C on a temperature regulated hot plate, stirring, for 2 weeks. At the end of the reaction, the mineral suspension was centrifuged at 4000 rpm, the liquid removed with a 2-inch needle, and carbon disulfide (CS_2) was introduced from a stock under N_2 atmosphere to solubilize the unreacted orthorhombic sulfur. The suspension was centrifuged once again and CS_2 removed prior to washing of the suspension with water (see below).

After synthesis, minerals in solution were spun at 4000 rpm for 10 min. while still sealed in glass serum bottles. Liquid was removed with a 2-inch needle while N_2 was being injected into the headspace using a second needle to maintain atmospheric pressure. Anoxic ultrapure water was added to the mineral suspension, and centrifugation repeated until the suspension had been washed twice. Then, vials were moved into the glovebox where the stoppers were removed. The serum bottles were covered with a paper tissue held in place by rubber bands. They were then placed in the vacuum chamber of the

glovebox under a vacuum of -0.8 mbar until dried. Dried samples were stored in stoppered, N_2-filled glass bottles at room temperature until further use.

All glassware used in the above protocols was acid washed for at least 24 hours in 1N HCl. This was followed by a 24-hour soak in ultrapure water, followed by 3 rinses in fresh ultrapure water.

Embedding and Polishing

Dried samples of synthetic mineral grains were sprinkled into plastic one-inch diameter rounds either on the bench or inside a glovebox (90% N_2/10% H_2). Samples were then immediately placed under vacuum within a Polyvac vacuum impregnator (Presi GmbH) at 80 kPa for 15 min. Then, Araldite epoxy 2020 A/B was slowly added (100:35 vol) until the sample was covered. Embedding proceeded at 80 kPa for 90 minutes. Samples were left to set for 24 hours before removing from the impregnator.

Embedded samples were first ground with abrasive papers: 1200 (15 micron), then 2500 (8 micron) using a PRESI Mecatech 334. Polishing utilized a PRESI diamond stick LD 33 (3 micron) and Presi RAM polishing cloth, followed by a final polish with 0.05 micron deagglomerated gamma alumina on a Buehler Chemomet I cloth (BUEHLER Micropolisch II 0.05 micron). Sample mounts were stored and transported in a nitrogen atmosphere. Just prior to synchrotron-based microanalysis, samples were polished with a 1 μm cloth to remove oxidized coatings.

Bulk Analysis

Particle size of synthesized samples was analyzed with a Mastersizer 2000 (Malvern Instruments GmbH). The surface area of solids was analyzed using a Micromeritics ASAP 2000 BET analyzer. Dried samples were loaded onto a holder and kept anoxic (100% N_2) until directly before analysis by μ-X-ray Diffraction (XRD) on a Bruker D8 Discover instrument (Bruker, Germany) equipped with a CoKα X-ray tube (k = 0.17902 nm, 30 kV, 30 mA) and GADDS area detector (Berthold et al., 2009). Mineral phases were identified using the International Center for Diffraction Data (ICDD) database.

Bulk trace element measurements were carried out by ICP-OES (Perkin Elmer Optima 5300 or Horiba Ultima 2) or an ICP-AES at University of Tübingen. Mineral samples (5-30 mg) were digested with aqua regia: 0.5 ml concentrated trace metal grade (TMG) HNO_3 (65%) and 1.5 mL concentrated HCl at 60°C. Residues were resuspended in 8N TMG HNO_3, and diluted ten-fold in 2% TMG HNO_3. Elemental sulfur that did not dissolve was filtered through a 0.2 μm Whatman filter. Aqueous samples were preserved with and further diluted in 2% TMG HNO_3.

Microscale Analysis & Spectroscopy

Elemental mapping by micro X-ray fluorescence (μXRF) and S and Fe K-edge X-ray absorption near-edge structure (XANES) spectroscopy was performed at beam lines (BL) 14-3 and 2-3, respectively at Stanford Synchrotron Radiation Lightsource (SSRL). Sulfur distribution was mapped in approximately 1x1 mm areas at ~2500 eV on BL14-3, which has an energy range of 2100 to 5000 eV. The incident energy was selected using a Si(111) ϕ=90 double crystal monochromator and the fluorescence signal was collected with a Si-drift diode Vortex detector (Hitachi) coupled to an Xspress3 pulse processing

system (Quantum Detectors). The energy was calibrated to the thiosulfate pre-edge peak set to 2472.02 eV or a sulfate peak from $CaSO_4$ set to 2483 eV. The spot size was 5x5 µm, unless otherwise noted, and dwell times were between 50 to 200 µs. For a subset of samples, S maps were collected at multiple energies (ME) around the S K-edge that corresponded to characteristic absorption features for monosulfides, pyrite, elemental sulfur, sulfite/metal monosulfides, sulfate, and total sulfur, in order of increasing energy. In 2013 these energies were 2470, 2471.5, 2472.5, 2476.5, 2483, and 2490 eV. In 2014 they were 2469.7, 2471.2, 2472.2, 2476.2, 2482.7, and 2499 eV. In 2015 and 2016 these energies were 2470.7, 2471.1, 2472.6, 2478.5, 2482.5 and 2499 eV. These maps were then deadtime corrected, and subjected to a principle component analysis (PCA) in the Microanalysis Toolkit (http://smak.sams-xrays.com) (Webb 2011). Compositionally diverse spots based on the absorption at different energies above the S K-edge were revealed by PCA, and these spots were chosen for S K-edge spectroscopy. Fluorescence spectra were collected from 2460 to 2500 eV. Spectra were deadtime corrected and normalized using the SIXPACK software package (Webb 2005). Within SIXPACK, the collected spectra from each sample (3 to 23 spectra per sample) were subjected to PCA to reveal the number of unique spectra. These end-members (EM), representing the compositional heterogeneity of all µXANES from an individual sample, were then fitted with spectra of reference sulfur compounds available from the ESRF (https://www.esrf.eu/home/UsersAndScience/Experiments/XNP/ID21/php.html), and additional samples from mineral collections of laboratory synthesis that were analyzed on BL 14-3 (these include mackinawite (FeS) and polysulfide). Mackinawite was bulk dried powder from the FeS_m synthesis described above, without added metals. The distribution

of EM were then back-mapped using the characteristic fluorescence intensities at the specific energies in the MicroAnalysis Toolkit, similar to published methods (Mayhew et al. 2011; Farfan et al. 2018).

Iron, sulfur, and trace metals were mapped in approximately 0.5x0.5 mm areas at 8500 eV on BL2-3, which has an energy range of 4500 to 24000 eV. The incident energy was selected using a Si(111) ϕ=0 double crystal monochromator, and the fluorescence signal was collected with a Si-drift diode Vortex detector (Hitachi) coupled to an Xspress3 pulse processing system (Quantum Detectors). The energy was calibrated using the first inflection of an Fe^0 foil as a standard (7112 eV). The spot size was either 2x2 or 5x5 μm, and dwell times were between 50 to 200 μs. Spots with different element intensities were chosen for Fe K-edge XANES (3 to 10 spectra per sample). Data was processed as described above.

Reference spectra used for fitting Fe K-edge XANES have been previously published (O'Day et al. 2004). Additional reference spectra were for Fe XANES collected as bulk samples on BL 4-1 at SSRL. Powdered samples were analyzed in sandwiches of Kapton tape, or in Teflon holder windows sealed with Kapton tape. Where necessary, powders were diluted with boron nitride to reduce self-absorption effects. The XANES spectra were collected in transmission mode as well as in fluorescence mode using a Lytle detector. The E_0 of an Fe^0 metal foil placed behind the first transmission detector was adjusted to 7112 eV in order to energy calibrate the resulting spectra. Replicate spectra were then averaged and background subtracted in SIXPACK (Webb 2005).

Semi-quantitative analysis of elemental abundance was accomplished by calibrating to NIST-traceable standards of the elements of interest, which were deposited on mylar

films measured at the same detector distance, incident energy, dwell time, spot size, and detector gain as the samples. A calibration file was assembled containing the information from the standard maps in the MicroAnalysis Toolkit, and applied to the sample. Because the samples were in thick mounts, the sample thickness was approximated as the absorption length for the mineral host, either FeS_m or FeS_2. Because individual grains may be thinner, especially on the margins than this absorption thickness, it is important to emphasize that this approach is only semi-quantitative. The amount of element per area was converted to concentrations as mg metal per g sample assuming one absorption length of either FeS_m or pyrite as the sample depth. A mask was applied to the image to eliminate pixels that did not represent Fe- and S-containing particles, and the statistics were calculated on the selected pixels by the MicroAnalysis Toolkit.

Results

Characteristics of Synthesized Minerals

The bulk mineralogy of synthetic samples was determined by XRD. Reference minerals were mackinawite, greigite, pyrite, pyrrhotite, and elemental sulfur. Synthesized FeS_m matched diffraction patterns for mackinawite, with minor greigite and pyrrhotite (**Figure 1**). No peaks attributable to the iron oxides hematite, goethite, magnetite, or ferrihydrite were present (data not shown). The XRD pattern for FeS_m with no metals was very similar to that with added Co or Ni. Transformation of FeS_m with or without Co or Ni to pyrite via H_2S oxidation (Rickard 1997) did not produce pyrite. However, peaks for mackinawite were sharpest in the FeS_m sample with no metals that reacted the longest - 20 days - whereas FeS_m with either Co or Ni (reacted 4 d) had lower intensity peaks, the

weakest in the sample that contained Ni. Pyrite was synthesized from FeS_m both with and without Co or Ni using the sulfur oxidation protocol. Residual elemental sulfur was also detected in Co- and Ni-containing samples. The pyrite peaks had similar intensity irrespective of metal additions.

During synthesis with 0.1 L each of 0.6 M ferrous ammonium sulfate and Na_2S solutions, 5.27 g of FeS_m is calculated to have formed. FeS_m had a BET surface area of 25.96±0.29 m^2/g, within the range of values reported in the literature for similar methodologies. Other BET measurements on synthetic freeze-dried FeS_m resulted in 36.5 m^2/g (Rickard 1997), 16-21 m^2/g (Benning et al. 2000), and 47 m^2/g (Wolthers et al. 2003). Particle size ranged from 2 to 138 μm, with greater than 90% of particles being less than 10 μm. Pyrite synthesized by sulfur oxidation had a BET surface area of 13.84±0.21 m^2/g. The surface area of Co-containing pyrite synthesized by sulfur oxidation was 18.06±0.12 m^2/g.

The results of S K-edge XRF and S XANES mapping of FeS_m synthesized with Co or Ni are shown in **Figure 2**, with the composition and fitting results of identified EM spectra reported in **Table 1**. FeS_m synthesized without metals was not mapped at ME through the S K-edge, so a similar map is not available. However, grains synthesized without metals were composed of FeS and sulfate, based on analysis of the spot S XANES spectra (**Figure 3**; **Table 1**). The standard quenstedtite (a hydrated ferric sulfate, $Fe_2(SO_4)_3 \cdot 11H_2O$) was used as a proxy for the presence of an inorganic sulfate, as this fit all of the samples in the study requiring it fairly well. Substituting another sulfate mineral (e.g. anhydrite) did not change the fit significantly (e.g. more than 10% improvement on $\sum^2$ values; data not shown). It is important to note that inclusion of quenstedtite in the fit is not equivalent to detection of this mineral, as XANES is not a crystallographic

technique. The use of quenstedtite in fits rather estimates the amount of a inorganic sulfate-bearing phase (Zeng et al. 2013). The FeS_m synthesized in the presence of Co or Ni similarly were fit with FeS and sulfate (**Figure 2**). Although ME mapping was not performed at the Fe K-edge, Fe XANES from points on the FeS_m with added Co sample map were fit by FeS and pyrrhotite (**Table 2**). In this case, the FeS spectra used was collected from a bulk powder of the FeS_m synthesized without any metals. FeS_m with added Ni was fit with mostly FeS and some pyrrhotite.

The synthesized FeS_m was sensitive to oxidation during embedding, polishing and oxic handling during analysis. **Figure 3** shows the EM S XANES spectrum of the FeS_m embedded oxically, which was fit by the reference spectra for FeS (0.68) and sulfate (0.37) (**Table 1**). The EM spectra from FeS_m embedded anoxically also fit with FeS and sulfate, but polysulfide was also necessary for a good fit (**Figure 3; Table 1**). No ME map was collected, so it was not possible to assess the distribution of the phases. However, these spectra were determined to be representative of the ten individual XANES collected on each sample by a PCA in SIXPACK. The FeS_m with no metal sample was not analyzed at the Fe K-edge.

The results of S K-edge XRF and S XANES mapping on samples treated with the sulfur oxidation method are presented in **Figure 4**, with the EM spectra displayed and used to determine phase distributions, and the spectral fitting results reported in **Table 1**. The FeS_m with no metals added oxidized with the sulfur oxidation method resulted in predominately pyrite (**Figure 4a**). Minor amounts of FeS were present in this and Co- and Ni-containing samples (**Figure 4b and 4c**), visible as a shoulder at 2470 eV along the pyrite pre-edge absorption feature. Sulfate was also present, as with FeS_m samples.

No sulfur was detected by XRF/XANES, although it was observed by XRD (**Figure 1**). When Co was present, the grains were predominantly pyrite, with some polysulfide and residual FeS (**Figure 4b**). The matrix was composed of sulfur and polysulfide, which was not seen in the metal-free sample. When Ni was added, most grains were made of pyrite with some polysulfide, or pyrite with FeS (**Figure 4c**).

The FeS_m containing either Co or Ni treated with the H_2S oxidation pathway did not produce pyrite, according to S XANES and XRF. The composition of EM S XANES spectra determined fitting was FeS with minor sulfate (**Table 1**). The Fe XANES spectra fit with an FeS standard (**Table 2**).

Trace element additions

The elemental concentrations of solutions used to synthesize FeS_m were analyzed, but S was not calibrated, and Fe was often above the range of the calibration curve and could not be quantified (**Table 3**). The ferrous ammonium sulfate solutions with nickel chloride or cobalt chloride were measured before adding the sodium sulfide solution, and had a concentration of 65.28 mg/L (1112 μM) Ni, which was diluted by an equal volume of sodium sulfide solution to achieve ca. 500 μM Ni final concentration. The solution with Co had 223.2 mg/L (3878 μM) Co, and was also diluted by an equal volume of the sodium sulfide solution to achieve ca. 2000 μM Co.

The Fe content of bulk solids determined with ICP-OES increased after applying the H_2S oxidation protocol (**Table 3**). The Fe content was only quantified in the Ni-containing sample after sulfur oxidation, due to the range of ICP-AES and standard concentrations. For the Co and Ni-bearing solids, Co and Ni were quantified in bulk by either ICP-OES

(FeS$_m$ and H_2S oxidation samples) or ICP-AES (sulfur oxidation samples; **Table 3**) or semi-quantitatively mapped by X-ray fluorescence at 11 keV on individual pixels (**Table 4**). The measured values of Co and Ni in FeS$_m$, measured by ICP-OES were 1.05±0.26 mg Ni per g FeS$_m$, and 3.71±0.06 mg Co per g FeS$_m$, higher than the range of the median values obtained by synchrotron-based XRF mapping on beam line 2-3 at 11 keV: of 0.4±0.2 mg Ni per g FeS$_m$ and 3.1±0.7 mg Co per g FeS$_m$. Quantification of Ni after sulfur oxidation diverged the most between methods. ICP-AES measured 3.4±0.1 mg Ni per g mineral, while XRF maps contained median values of 0.5±0.4 mg Ni per g mineral. Results for Co after sulfur oxidation were comparable by bulk and microscale methods. Maps of particles used for XRF quantification are shown in **Supplementary Figure 1**.

Discussion

Mineral Transformation

For the FeS$_m$ synthesized in this study, XRD documented the mineral mackinawite, with minor greigite and pyrrhotite (**Figure 1**). The best fitting standard for S XANES spectra was with FeS, a mackinawite standard, occasional polysulfide, and varying amounts of sulfate (**Table 1**). Even after embedding in the glovebox, the FeS$_m$ still shows signs of oxidation, evidenced by the inclusion of sulfate and polysulfide in the fits, although it may be less oxidized than samples embedded in air (**Figure 3**). Less sulfate was needed to fit the anoxically embedded samples, however, indicating some success of the protection from oxygen. The presence of polysulfide may have resulted from some sample hydration during storage, as the sample was anoxically embedded a year after oxically embedded samples, although they were stored under dry N_2 in airtight

containers. As sulfate minerals were not detected in XRD (detection limit 5 wt. %), oxidation likely occurred during the storage, embedding or analysis of samples, and not during synthesis or transformation protocols. There was a major reflection at about 35° in the FeS_m that could be greigite or pyrite, but other major reflections for these minerals were absent. The addition of Co or Ni did not appear to alter the mineralogy of the FeS_m, or to change the intensity or width of reflections (**Figure 1**).

The attempts to transform FeS_m, with or without Co and/or Ni, to pyrite via H_2S oxidation were not successful. From XRD, the sample still appeared to be mackinawite, with the most intense reflections in the Co-containing samples (**Figure 1**). The Ni and Co-containing samples were only reacted 4 d, and yet had much more intense reflections for mackinawite than FeS_m without metals, reacted either 4 or 20 d. The failure of the H_2S oxidation method to produce pyrite from FeS_m synthesized with Co or Ni was also verified by S XANES and XRF mapping (**Table 1**), as well as by point Fe XANES analysis (**Table 2**). These results are consistent with a number of studies, which found very slow reactions between mackinawite and H_2S to form pyrite (Berner 1970; Schoonen and Barnes 1991b; Wilkin and Barnes 1996; Benning et al. 2000). It has been suggested that the freeze-dried FeS, used in the successful synthesis of pyrite via H_2S oxidation (Rickard 1997), underwent minor oxidation by oxygen during drying, providing oxidized surface sites for the formation of pyrite via reaction with H_2S (Benning et al. 2000). Secondary electron microscopy (SEM) studies of freeze-dried mackinawite in that second study noted an oxidized sulfate mineral phase, as well as a change in morphology from freshly-precipitated mackinawite (Benning et al. 2000). In this same study, the freeze-dried material produced pyrite in reaction with H_2S (100%

433 transformation after 9 days), whereas freshly precipitated mackinawite reacted with H_2S
434 did not. Our finding that N_2-dried mackinawite does not react with H_2S to form pyrite
435 further support the claim (i.e. Benning et al. 2000) that H_2S oxidation of mackinawite is
436 not a significant reaction in the formation of pyrite at low temperatures.
437 In contrast, pyrite was formed from the sulfur oxidation method, evident in clear
438 reflections for pyrite from XRD in metal-free samples (**Figure 1**). After pyritization,
439 most XRD reflections for mackinawite had disappeared, indicating near-complete
440 reaction. From the S ME mapping and EM XANES, pyrite was also the main product
441 (**Figure 4**; **Table 1**), with minor FeS and sulfate, likely reflecting oxidation during
442 sample mounting and/or analysis (e.g. **Figure 2**). The spot Fe XANES analysis also
443 documented pyrite, but the product still retained some FeS_m (**Table 4**). In addition,
444 marcasite was a component of Fe XANES fits (**Table 4**), which likely reflects the same
445 sulfur oxidation state and similar orbital energy levels of Fe in pyrite and marcasite
446 (Jones 2006), rather than the presence of marcasite. The Fe XANES of pyrite and
447 marcasite are very similar (O'Day et al. 2004). The inclusion of pyrrhotite in some fits
448 could reflect some oxidation during embedding, storage, or analysis.
449 Pyrite was also produced in the Co-containing solids, as evidenced by XRD, S XANES,
450 and Fe XANES. In the Co-containing samples, an additional intense reflection for sulfur
451 was present at about 26°, and several minor reflections between 30-35° in the XRD data
452 (**Figure 1**). These likely correspond to residual sulfur retained after CS_2 washing. The
453 single CS_2 wash must have been insufficient to remove sulfur. It is significant that
454 evidence for residual sulfur is not seen in the metal-free product. In Co-containing
455 samples analyzed by S XANES, FeS was still present in pyrite grains (visible as a

shoulder at 2470 eV), as was polysulfide **(Figure 4**). Sulfur and polysulfide comprised the matrix, consistent with the intense reflections for sulfur by XRD. Polysulfides form in reaction of elemental sulfur with water, and themselves react with FeS_m to form pyrite (Schoonen and Barnes 1991b), and so are expected S phases during pyrite formation by the S^0 oxidation method. By Fe XANES, both pyrite/marcasite and FeS were components of fits. Taken together, these data indicate that the presence of Co impeded reaction of FeS_m to pyrite in the time course of the experiments (2 weeks). Although FeS_m was still detectable in metal-free product, the absence of any detectable sulfur may signify that metal-free FeS_m reacted more completely than Co-amended FeS_m. Inhibition of FeS transformation to pyrite has been observed in the presence of arsenate [As(V)], although this is linked to arsenate oxidizing both Fe and S (Wolthers et al. 2007). An analogous pathway can be excluded for Co^{2+}, as its reduction in aqueous phase is unlikely. Arsenate and arsenite ([As(III)] can also prevent FeS transformation to pyrite by sorption and blockage of surface sites (Wolthers et al. 2007). Although, Co does not adsorb even as strongly to FeS as Ni (Morse and Arakaki 1993), yet Ni-containing FeS appears to have more completely reacted in our experiments (see below). The lower concentrations of Co in pyrite compared to FeS (Tables 3 and 4) indicate that some Co could have been mobilized from solid phases during the reaction and available for sorption. It is impossible to rule out inhibition of pyrite formation due to Co sorption with our data.

For Ni-containing samples, the predominant product of sulfur oxidation was pyrite, based on XRD, S XANES, and Fe XANES analyses. Some residual FeS_m was present based on S and Fe XANES (**Tables 1** and **2**). One Fe XANES EM also fit with maghemite, indicating Fe oxidation, which likely occurred during sample embedding, storage, or

analysis, as it was not detected by XRD prior to these steps. Sulfur was also present based on XRD, but the diffraction peaks were not as sharp or as large as for the Co-containing product. Polysulfide was detectable in S XANES (**Figure 4**). The reaction of FeS_m to pyrite also seems to be incomplete in the presence of Ni, but may have progressed further given the evidence for more abundant sulfur/polysulfide in the Co-containing grains. Another line of evidence is the more abundant distribution of sulfur-rich grains in Co-containing product, as revealed by the 8000 eV XRF map (**Supplementary Figure 2**) as compared to the Ni-containing product, although the sample size is just a few grains. These results of incomplete pyrite formation in Ni-containing samples are in contrast to the recent observation that the presence of Ni accelerates the rate of pyrite formation (Morin et al. 2017). In that work, pyrite was formed from *de novo* synthesis from slightly acidic (ca. pH = 5.5) solutions of ferric chloride and H_2S (Noël et al. 2014, 2015). In this mechanism, Fe(III) must be the oxidant, whereas our protocol started with solid FeS_m and utilized sulfur as the oxidant. The authors proposed that Ni impurities accelerated pyrite nucleation from solution (Morin et al. 2017), which is generally slow. However, formation of pyrite in marine sediments likely proceeds from the nucleation and subsequent sulfidization of FeS minerals, such as mackinawite and greigite (Schoonen and Barnes 1991a), rather than through reaction of aqueous Fe(III) and H_2S. This inference is supported by the observation of FeS phases being converted to pyrite with depth in numerous anoxic sediments (Cutter and Velinsky 1988; Huerta-Diaz and Morse 1992; Scholz and Neumann 2007). Our experiments therefore suggest that Ni (and Co) impurities might impede the rate of pyritization in pH circumneutral sediments, although

501 others note that Ni and Co may more completely pyritize than other metals (Morgan et al.
502 2012b).

503 The weight percent of Fe in FeS_m calculated from bulk digestion data in **Table 3** was
504 about 30-40%, less than the predicted 63.5% for a 1:1 Fe:S stoichiometry. This lower
505 weight percent iron may have been caused by sulfate precipitation during drying, as
506 discussed above. After the H_2S oxidation protocol, the weight percent of iron increased to
507 42-51%, closer to stoichiometric FeS, but still lower than expected. This may be due to
508 increasing crystallinity of the FeS_m in aqueous phase (Rickard 1995), which has support
509 from the sharpening of diffraction peaks (**Figure 1**), or washing out of excess sulfate with
510 the fluids used for H_2S oxidation. Although the Fe content was not determined on most
511 solids produced by the sulfur oxidation protocol, the Fe content for pyrite for the Ni-
512 containing sample was ca. 33 wt %, whereas stoichiometric pyrite should have 46.55%
513 Fe. This likely reflects residual sulfur in the solid sample after the sulfur oxidation
514 method, as well as the persistence of FeS_m.
515

516 **Trace Element Incorporation**

517 The distribution coefficient for Co in FeS_m at 25°C is 29±3 (Morse and Arakaki, 1993),
518 which predicted 16±2 mg Co per g FeS_m in our synthesized mineral. The measured
519 values of Co were 2.6 to 3.7 mg Co per g mineral were well under this range. Based on
520 the published distribution coefficient of 280±181 for Ni in FeS_m at 25°C (Morse and
521 Arakaki 1993), we expected to see 3.9±2.5 mg Ni/g FeS_m. The measured value of Ni in
522 FeS_m (0.6 to 1.05 mg Ni/g mineral) was below this range (**Table 3**). In those experiments,
523 mackinawite was synthesized by slow titration, whereas our FeS_m was synthesized

524 rapidly by mixing a Co- or Ni-bearing iron solution with a sulfide solution. It is likely
525 that this fast precipitation did not allow full uptake of the likely equilibrium values of Co
526 and Ni observed in slow precipitation experiments (Morse and Arakaki 1993). This may
527 be due to the slower exchange of H_2O ligand for S^{2-} on Co^{2+} and Ni^{2+} ions as compared to
528 Fe^{2+} ions (Morse and Luther III 1999).
529 After the H_2S oxidation protocol, the measured value was 4.05±1.92 mg Co per g
530 mineral, and 1.1 mg Co per g mineral after the sulfur oxidation protocol. Cobalt
531 enrichments in FeS_m are generally present in all particles based on XRF mapping of the
532 synthesized minerals at 8500 eV (**Supplementary Figure 2**). In the samples mapped
533 after sulfur oxidation, Co was distributed throughout the Fe-rich particles. From cross-
534 plots of the Fe and S pixels, the Fe-rich particles always contain some S, and so are
535 inferred to be FeS_m/pyrite. The sulfur-rich grains comprise a very low-Fe population of
536 pixels, and are likely sulfur/polysulfide-rich grains (analyses not shown). Cobalt is visible
537 in the FeS_m/pyrite grains, but absent in the sulfur/polysulfide grains, indicating that Co is
538 preferentially incorporated into sulfide minerals. From the bulk (ICP-OES or ICP-AES)
539 and XRF metal quantification, there was general agreement between the techniques for
540 the quantity of Co in both FeS_m and sulfur oxidation products (**Figure 5**). However, Co
541 was quantitatively lost from the samples during transformation. The lower concentration
542 of Co in Fe-rich particles by XRF after pyrite transformation (**Supplementary Figures 1**
543 **and 2**) indicates this is not a phenomenon of solid-phase dilution with residual sulfur for
544 the ICP analyses. Therefore, it seems likely that Co is lost from the sulfide phase during
545 transformation of FeS_m to pyrite.

After treating FeS_m with the H_2S oxidation protocol, Ni increased to 1.43±0.87 mg Ni per g mineral. The amount in pyrite produced from the sulfur oxidation protocol was 3.4±0.1 mg Ni per g mineral. In Ni-containing samples, the FeS_m has Ni distributed throughout all grains. In the Ni-containing product oxidized by sulfur, both S and Fe-rich grains are visible in the XRF map, similar to the Co-containing sample (**Supplementary Figure 2**). In the product, some Fe-rich grains are preferentially enriched in Ni, while others are Ni-poor, distinct from the Co-rich product. The S-rich grains have little Ni. As no multi-energy maps were made at these higher energies on BL2-3 (e.g. the Fe K-edge), it is not possible to say whether Ni preferentially incorporated into discrete iron sulfide phases, such as FeS_m or pyrite. Other studies have documented a preference of Ni for the pyrite vs. mackinawite mineral (Noël et al. 2015). This may be consistent with preferential Ni concentration in pyrite-bearing grains, as opposed to FeS_m grains, although we cannot validate this with the current dataset. The ICP data always detected more Ni in the samples than is apparent with the synchrotron-based XRF maps (**Figure 5**), likely indicating the need for further matrix correction for XRF standards. Both techniques show an increase of Ni in the solid after sulfur oxidation, although this increase is unlikely to be statistically significant in the XRF data. It is possible that in case of dissolution of FeS, and incomplete pyrite formation, mobilized Ni was effectively sequestered in fewer grains, increasing the concentration.

A final observation is that the addition of Co or Ni shifted the pre-edge peak position of the FeS in the S XANES spectra to more positive values (**Figure 6**), which was more extreme for Ni. A similar peak shift was noted for pyrite, although only for Ni. Other authors noted longer bond distance (2.28 Å) for Ni-S than for Fe-S (2.26 Å) based on Ni

569 EXAFS of mackinawite synthesized with Ni (Wilkin and Beak 2017). However, shorter
570 bond distances generally require higher excitation energy. It may more likely reflect the
571 ordering of stability constants of the transition metal series, e.g. the Irving-Williams
572 order, Fe<Co<Ni<Cu>Zn (Rickard and Luther III 2006). Although the amount of the
573 non-Fe metal is small, these pre-edge peaks may reflect the increased energy needed to
574 achieve electronic transitions to empty hybridized Me-S and S-S anti-bonding orbitals.
575

576 **Implications**

577 The experiments described herein attempt to determine how efficiently the trace elements
578 Ni and Co are pyritized under low-temperature pyrite formation from mackinawite. A
579 first and important result was that oxidation of FeS_m by H_2S did not produce pyrite,
580 casting doubt on the validity of this as a pyrite formation pathway in the absence of
581 oxidized surface sites. However, pyrite was successfully synthesized through oxidation of
582 FeS_m with elemental sulfur. The equilibrium concentration of Co and Ni in the initial
583 FeS_m predicted by the published distribution coefficients was not attained in our
584 experiments due to the fast precipitation method used. Cobalt was lost from the solid
585 during transformation, as evidenced by the diminished concentrations of Co in pyrite
586 compared to FeS_m. The concentration of Ni increased during transformation, possibly due
587 to the dissolution of FeS_m and preferential sequestration of Ni in pyrite. In both cases,
588 pyrite formation was not complete in the presence of added metals, indicating a kinetic
589 inhibition to the formation of pyrite in the presence of Co and Ni. Taken together, these
590 results suggest that if the pyrite formation pathway can be determined to initiate from a
591 precursor FeS phase, the concentration of Co in pyrite could serve as a conservative

592 record of environmental concentrations. Nickel, however, seems unreliable in this
593 capacity, as pyrite appears to take up additional Ni in comparison to precursor FeS_m,
594 during its formation, as well as incorporate in other phases, such as elemental sulfur. A
595 caveat of this work is that other pyrite formation mechanisms are possible, e.g. from
596 another solid-phase precursor mineral such as greigite or by reductive dissolution of
597 Fe(III) (oxyhydr)oxides with hydrogen sulfide, or an aqueous or colloidal species (e.g.
598 FeS_{aq}), and the fate of trace metals during transformation should also be evaluated under
599 those conditions. Also, our results are specific only to Co and Ni, and should not be
600 extrapolated to other metals.

601 **Acknowledgements**

602 We thank Ellen Roehm for performing BET, Mastersizer and ICP-AES analysis of
603 samples. James Byrne and Maximilian Halama analyzed samples by μXRD. Stefan
604 Peiffer and Mali Wan gave helpful advice regarding the synthesis of pyrite. Tabea
605 Schmid and Bertrand Ligous assisted in developing and performing the epoxy embedding
606 and polishing of samples. The polysulfide standard was a gift of Greg Druschel and
607 Fotios Kafantaris. Sümeyya Eroglu, Maximilian Halama, and Aude Picard assisted with
608 measurements at the SSRL. Courtney Roach assisted with beam line optimization and
609 data interpretation. This work was funded by a Deutsche Forschungsgemeinschaft grant
610 (KA 1736/24-1). Use of the Stanford Synchrotron Radiation Lightsource, SLAC National
611 Accelerator Laboratory, is supported by the U.S. Department of Energy, Office of
612 Science, Office of Basic Energy Sciences under Contract No. DE-AC02-76SF00515.

613

614 **References**
615
616 Algeo, T.J., and Maynard, J.B. (2004) Trace-element behavior and redox facies in core shales of

617 Upper Pennsylvanian Kansas-type cyclothems. Chemical Geology, 206, 289–318.

618 Algeo, T.J., and Rowe, H. (2012) Paleoceanographic applications of trace-metal concentration
619 data. Chemical Geology, 324–325, 6–18.

620 Anbar, A.D., and Knoll, A.H. (2002) Proterozoic ocean chemistry and evolution: a bioinorganic
621 bridge? Science, 297.

622 Benning, L.G., Wilkin, R.T., and Barnes, H.L. (2000) Reaction pathways in the Fe-S system
623 below 100°C. Chemical Geology, 167, 25–51.

624 Berner, R.A. (1970) Sedimentary pyrite formation. American Journal of Science, 286, 1–23.

625 Burton, E.D., Bush, R.T., Sullivan, L.A., Hocking, R.K., Mitchell, D.R.G., Johnston, S.G.,
626 Fitzpatrick, R.W., Raven, M., McClure, S., and Jang, L.Y. (2009) Iron-Monosulfide
627 Oxidation in Natural Sediments: Resolving Microbially Mediated S Transformations Using
628 XANES, Electron Microscopy, and Selective Extractions. Environmental Science &
629 Technology, 43, 3128–3134.

630 Butler, I.B., and Rickard, D. (2000) Framboidal pyrite formation via the oxidation of iron (II)
631 monosulfide by hydrogen sulphide. Geochimica et Cosmochimica Acta, 64, 2665–2672.

632 Canfield, D.E., and Farquhar, J. (2009) Animal evolution, bioturbation, and the sulfate
633 concentration of the oceans. Proc Natl Acad Sci U S A, 106, 8123–8127.

634 Chappaz, A., Lyons, T.W., Gregory, D.D., Reinhard, C.T., Gill, B.C., Li, C., and Large, R.R.
635 (2014) Does pyrite act as an important host for molybdenum in modern and ancient euxinic
636 sediments? Geochimica et Cosmochimica Acta, 126, 112–122.

637 Chi Fru, E., Rodríguez, N.P., Partin, C.A., Lalonde, S. V, Andersson, P., Weiss, D.J., El Albani,
638 A., Rodushkin, I., and Konhauser, K.O. (2016) Cu isotopes in marine black shales record
639 the Great Oxidation Event. Proceedings of the National Academy of Sciences, 113, 4941
640 LP-4946.

641 Cutter, G.A., and Velinsky, D.J. (1988) Temporal variations of sedimentary sulfur in a Delaware
642 salt marsh. Marine Chemistry, 23, 311–327.

643 Dupont, C.L., Yang, S., Palenik, B., and Bourne, P.E. (2006) Modern proteomes contain putative
644 imprints of ancient shifts in trace metal geochemistry. Proceedings of the National Academy
645 of Sciences, 103, 17822–17827.

646 Dupont, C.L., Butcher, A., Valas, R.E., Bourne, P.E., and Caetano-Anoll√©s, G. (2010) History
647 of biological metal utilization inferred through phylogenomic analysis of protein structures.
648 Proceedings of the National Academy of Sciences, 107, 10567–10572.

649 Fakhraee, M., Crowe, S.A., and Katsev, S. (2018) Sedimentary sulfur isotopes and Neoarchean
650 ocean oxygenation. Science Advances, 4.

651 Farfan, G.A., Apprill, A., Webb, S.M., and Hansel, C.M. (2018) Coupled X-ray Fluorescence and
652 X-ray Absorption Spectroscopy for Microscale Imaging and Identification of Sulfur Species
653 within Tissues and Skeletons of Scleractinian Corals. Analytical Chemistry, 90, 12559–

12566.

Frierdich, A.J., Luo, Y., and Catalano, J.G. (2011) Trace element cycling through iron oxide minerals during redox-driven dynamic recrystallization. Geology, 39, 1083–1086.

Goldhaber, M.B., and Kaplan, I.R. (1974) The sulfur cycle. In E.D. Goldberg, Ed., The Sea Vol. 5, pp. 569–655. Wiley-Interscience, New York, N.Y.

Gregory, D.D., Large, R.R., Halpin, J.A., Baturina, E.L., Lyons, T.W., Wu, S., Danyushevsky, L., Sack, P.J., Chappaz, A., Maslennikov, V. V, and others (2015) Trace Element Content of Sedimentary Pyrite in Black Shales*. Economic Geology, 110, 1389–1410.

Harrison, W., Pevear, D., and Lindahl, P. (1973) Trace Elements in Pyrites of the Green River Formation Oil Shales, Wyoming, Utah, and Colorado. In M. Tuttle, Ed., Geochemical, Biogeochemical, and Sedimentological Studies of the Green River Formation, Wyoming, Utah, and Colorado pp. D1–D23. U.S. Geological Survey.

Hellige, K., Pollok, K., Larese-Casanova, P., Behrends, T., and Peiffer, S. (2012) Pathways of ferrous iron mineral formation upon sulfidation of lepidocrocite surfaces. Geochimica et Cosmochimica Acta, 81, 69–81.

Holland, H.D. (1984) The Chemical Evolution of the Atmosphere and Oceans. Princeton University Press, Princeton, NJ.

Huerta-Diaz, M.A., and Morse, J.W. (1990) A quantitative method for determination of trace metal concentrations in sedimentary pyrite. Marine Chemistry, 29, 119–144.

——— (1992) Pyritization of trace metals in anoxic marine sediments. Geochimica et Cosmochimica Acta, 56, 2681–2702.

Hunger, S., and Benning, L.G. (2007) Greigite: a true intermediate on the polysulfide pathway to pyrite. Geochemical Transactions, 8, 1.

Jones, R.T. (2006) Electronic Structures of the Sulfide Minerals Sphalerite, Wurtzite, Pyrite, Marcasite, and Chalcopyrite. University of South Australia.

Jørgensen, B.B. (1982) Mineralization of organic matter in the sea bed—the role of sulphate reduction. Nature, 296, 643.

Keene, A.F., Johnston, S.G., Bush, R.T., Sullivan, L.A., Burton, E.D., McElnea, A.E., Ahern, C.R., and Powell, B. (2011) Effects of hyper-enriched reactive Fe on sulfidisation in a tidally inundated acid sulfate soil wetland. Biogeochemistry, 103, 263–279.

Konhauser, K.O., Pecoits, E., Lalonde, S. V, Papineau, D., Nisbet, E.G., Barley, M.E., Arndt, N.T., Zahnle, K., and Kamber, B.S. (2009) Oceanic nickel depletion and a methanogen famine before the Great Oxidation Event. Nature, 458, 750–753.

Konhauser, K.O., Lalonde, S. V, Planavsky, N.J., Pecoits, E., Lyons, T.W., Mojzsis, S.J., Rouxel, O.J., Barley, M.E., Rosiere, C., Fralick, P.W., and others (2011) Aerobic bacterial pyrite oxidation and acid rock drainage during the Great Oxidation Event. Nature, 478, 369–373.

690 Kraal, P., Burton, E.D., and Bush, R.T. (2013) Iron monosulfide accumulation and pyrite
691 formation in eutrophic estuarine sediments. Geochimica et Cosmochimica Acta, 122, 75–88.

692 Large, R.R., Danyushevsky, L., Hollit, C., Maslennikov, V., Meffre, S., Gilbert, S., Bull, S.,
693 Scott, R., Emsbo, P., Thomas, H., and others (2009) Gold and Trace Element Zonation in
694 Pyrite Using a Laser Imaging Technique: Implications for the Timing of Gold in Orogenic
695 and Carlin-Style Sediment-Hosted Deposits. Economic Geology, 104, 635–668.

696 Large, R.R., Halpin, J.A., Danyushevsky, L. V, Maslennikov, V. V, Bull, S.W., Long, J.A.,
697 Gregory, D.D., Lounejeva, E., Lyons, T.W., Sack, P.J., and others (2014) Trace element
698 content of sedimentary pyrite as a new proxy for deep-time ocean–atmosphere evolution.
699 Earth and Planetary Science Letters, 389, 209–220.

700 Long, J.A., Large, R.R., Lee, M.S.Y., Benton, M.J., Danyushevsky, L. V, Chiappe, L.M., Halpin,
701 J.A., Cantrill, D., and Lottermoser, B. (2016) Severe selenium depletion in the Phanerozoic
702 oceans as a factor in three global mass extinction events. Gondwana Research, 36, 209–218.

703 Luther, G.W., and Rickard, D.T. (2005) Metal sulfide cluster complexes and their
704 biogeochemical importance in the environment. Journal of Nanoparticle Research, 7, 389–
705 407.

706 Mayhew, L.E., Webb, S.M., and Templeton, A.S. (2011) Microscale Imaging and Identification
707 of Fe Speciation and Distribution during Fluid-Mineral Reactions under Highly Reducing
708 Conditions. Environmental Science & Technology, 45, 4468–4474.

709 Mojzsis, S.J., Coath, C.D., Greenwood, J.P., McKeegan, K.D., and Harrison, T.M. (2003) Mass-
710 independent isotope effects in Archean (2.5 to 3.8 Ga) sedimentary sulfides determined by
711 ion microprobe analysis. Geochimica et Cosmochimica Acta, 67, 1635–1658.

712 Morgan, B., Burton, E.D., and Rate, A.W. (2012a) Iron monosulfide enrichment and the presence
713 of organosulfur in eutrophic estuarine sediments. Chemical Geology, 296–297, 119–130.

714 Morgan, B., Rate, A.W., and Burton, E.D. (2012b) Trace element reactivity in FeS-rich estuarine
715 sediments: Influence of formation environment and acid sulfate soil drainage. Science of
716 The Total Environment, 438, 463–476.

717 Morin, G., Noël, V., Menguy, N., Brest, J., Baptiste, B., Tharaud, M., Ona-Nguema, G., Ikogou,
718 M., Viollier, E., and Juillot, F. (2017) Nickel accelerates pyrite nucleation at ambient
719 temperature . Geochemical Perspectives Letters, 5, 6–11.

720 Morse, J.W., and Arakaki, T. (1993) Adsorption and coprecipitation of divalent metals with
721 mackinawite (FeS). Geochimica et Cosmochimica Acta, 57, 3635–3640.

722 Morse, J.W., and Luther III, G.W. (1999) Chemical influences on trace metal-sulfide interactions
723 in anoxic sediments. Geochimica et Cosmochimica Acta, 63, 3373–3378.

724 Noël, V., Marchand, C., Juillot, F., Ona-Nguema, G., Viollier, E., Marakovic, G., Olivi, L.,
725 Delbes, L., Gelebart, F., and Morin, G. (2014) EXAFS analysis of iron cycling in mangrove
726 sediments downstream a lateritized ultramafic watershed (Vavouto Bay, New Caledonia).
727 Geochimica et Cosmochimica Acta, 136, 211–228.

Noël, V., Morin, G., Juillot, F., Marchand, C., Brest, J., Bargar, J.R., Muñoz, M., Marakovic, G., Ardo, S., and Brown Jr, G.E. (2015) Ni cycling in mangrove sediments from New Caledonia. Geochimica et Cosmochimica Acta, 169, 82–98.

O'Day, P.A., Rivera Jr., N., Root, R., and Carroll, S.A. (2004) X-ray absorption spectroscopic study of Fe reference compounds for the analysis of natural sediments. American Mineralogist, 89, 572–585.

Olson, L., Quinn, K.A., Siebecker, M.G., Luther, G.W., Hastings, D., and Morford, J.L. (2017) Trace metal diagenesis in sulfidic sediments: Insights from Chesapeake Bay. Chemical Geology, 452, 47–59.

Partin, C.A., Lalonde, S. V, Planavsky, N.J., Bekker, A., Rouxel, O.J., Lyons, T.W., and Konhauser, K.O. (2013) Uranium in iron formations and the rise of atmospheric oxygen. Chemical Geology, 362, 82–90.

Peiffer, S., Behrends, T., Hellige, K., Larese-Casanova, P., Wan, M., and Pollok, K. (2015) Pyrite formation and mineral transformation pathways upon sulfidation of ferric hydroxides depend on mineral type and sulfide concentration. Chemical Geology, 400, 44–55.

Rickard, D. (1995) Kinetics of FeS precipitation: Part 1. Competing reaction mechanisms. Geochimica et Cosmochimica Acta, 59, 4367–4379.

Rickard, D. (1997) Kinetics of pyrite formation by the H2S oxidation of iron (II) monosulfide in aqueous solutions between 25 and 125C: the rate equation. Geochimica et Cosmochimica Acta, 61, 115–134.

Rickard, D., and Luther III, G.W. (2006) Metal Sulfide Complexes and Clusters. Reviews in Mineralogy and Geochemistry, 61, 421–504.

Rickard, D., and Luther III, G.W. (2007) Chemistry of Iron Sulfides. Chemical Reviews, 107, 514–562.

Rickard, D., and Morse, J.W. (2005) Acid volatile sulfide (AVS). Marine Chemistry, 97, 141–197.

Rickard, D.T. (1969) The chemistry of iron sulfide formation at low temperatures. Stockholm Contributions to Geology, 20, 67–95.

Rickard, D.T., and Luther III, G.W. (1997) Kinetics of pyrite formation by the H2S oxidation of iron(II) monosulfide in aqueous solutions between 25 and 125C: The mechanism. Geochimica et Cosmochimica Acta, 61, 135–147.

Robbins, L.J., Lalonde, S. V, Saito, M.A., Planavsky, N.J., Mloszewska, A.M., Pecoits, E., Scott, C., Dupont, C.L., Kappler, A., and Konhauser, K.O. (2013) Authigenic iron oxide proxies for marine zinc over geological time and implications for marine eukaryotic metallome evolution. Geobiology, 11, 295–306.

Robbins, L.J., Lalonde, S. V, Planavsky, N.J., Partin, C.A., Reinhard, C.T., Kendall, B., Scott, C., Hardisty, D.S., Gill, B.C., Alessi, D.S., and others (2016) Trace elements at the intersection of marine biological and geochemical evolution. Earth-Science Reviews, 163, 323–348.

766 Rouxel, O.J., Bekker, A., and Edwards, K.J. (2005) Iron Isotope Constraints on the Archean and
767 Paleoproterozoic Ocean Redox State. Science, 307, 1088–1091.

768 Scholz, F., and Neumann, T. (2007) Trace element diagenesis in pyrite-rich sediments of the
769 Achterwasser lagoon, SW Baltic Sea. Marine Chemistry, 107, 516–532.

770 Schoonen, M.A.A., and Barnes, H.L. (1991a) Reactions forming pyrite and marcasite from
771 solution: I. Nucleation of FeS2 below 100°C. Geochimica et Cosmochimica Acta, 55, 1495–
772 1504.

773 ——— (1991b) Reactions forming pyrite and marcasite from solution: II. Via FeS precursors
774 below 100°C. Geochimica et Cosmochimica Acta, 55, 1505–1514.

775 Scott, C., Lyons, T.W., Bekker, A., Shen, Y., Poulton, S.W., Chu, X., and Anbar, A.D. (2008)
776 Tracing the stepwise oxygenation of the Proterozoic ocean. Nature, 452, 456–459.

777 Scott, C., Planavsky, N.J., Dupont, C.L., Kendall, B., Gill, B.C., Robbins, L.J., Husband, K.F.,
778 Arnold, G.L., Wing, B.A., Poulton, S.W., and others (2012) Bioavalability of zinc in marine
779 systems through time. Nature Geoscience, 6, 125–128.

780 Shen, Y., Buick, R., and Canfield, D.E. (2001) Isotopic evidence for microbial sulphate reduction
781 in the early Archaean era. Nature, 410, 77–81.

782 Swanner, E.D., Bekker, A., Pecoits, E., Konhauser, K.O., Cates, N.L., and Mojzsis, S.J. (2013)
783 Geochemistry of pyrite from diamictites of the Boolgeeda Iron Formation, Western
784 Australia with implications for the GOE and Paleoproterozoic ice ages. Chemical Geology,
785 362, 131–142.

786 Swanner, E.D., Planavsky, N.J., Lalonde, S. V., Robbins, L.J., Bekker, A., Rouxel, O.J., Saito,
787 M.A., Kappler, A., Mojzsis, S.J., and Konhauser, K.O. (2014) Cobalt and marine redox
788 evolution. Earth and Planetary Science Letters, 390, 253–263.

789 Sweeney, R.E. (1972) Pyritization during diagenesis of marine sediments. Department of
790 Geology. University of California, Los Angeles.

791 Tardani, D., Reich, M., Deditius, A.P., Chryssoulis, S., Sánchez-Alfaro, P., Wrage, J., and
792 Roberts, M.P. (2017) Copper–arsenic decoupling in an active geothermal system: A link
793 between pyrite and fluid composition. Geochimica et Cosmochimica Acta, 204, 179–204.

794 Tostevin, R., Turchyn, A. V, Farquhar, J., Johnston, D.T., Eldridge, D.L., Bishop, J.K.B., and
795 McIlvin, M. (2014) Multiple sulfur isotope constraints on the modern sulfur cycle. Earth
796 and Planetary Science Letters, 396, 14–21.

797 Wan, M., Schröder, C., and Peiffer, S. (2017) Fe(III):S(-II) concentration ratio controls the
798 pathway and the kinetics of pyrite formation during sulfidation of ferric hydroxides.
799 Geochimica et Cosmochimica Acta, 217, 334–348.

800 Wang, Q., and Morse, J.W. (1996) Pyrite formation under conditions approximating those in
801 anoxic sediments I. Pathway and morphology. Marine Chemistry, 52, 99–121.

802 Webb, S.M. (2005) SIXpack: a graphical user interface for XAS analysis using IFEFFIT. Physica

Scripta, 2005, 1011.

——— (2011) The MicroAnalysis Toolkit: X-ray fluorescence image processing. In AIP Conference Proceedings Vol. 1365, pp. 196–199.

Wilkin, R.T., and Barnes, H.L. (1996) Pyrite formation by reactions of iron monosulfides with dissolved inorganic and organic sulfur species. Geochimica et Cosmochimica Acta, 60, 4167–4179.

Wilkin, R.T., and Beak, D.G. (2017) Uptake of nickel by synthetic mackinawite. Chemical Geology, 462, 15–29.

Wolthers, M., Van der Gaast, S.J., and Rickard, D. (2003) The structure of disordered mackinawite. American Mineralogist, 88, 2007–2015.

Wolthers, M., Butler, I.B., and Rickard, D. (2007) Influence of arsenic on iron sulfide transformations. Chemical Geology, 236, 217–227.

Zeng, T., Arnold, W.A., and Toner, B.M. (2013) Microscale Characterization of Sulfur Speciation in Lake Sediments. Environmental Science & Technology, 47, 1287–1296.

Figure Captions

Figure 1. XRD of a. FeS with and without Co and/or Ni, b. FeS with and without Co and/or Ni after pyrite synthesis for 4 or 20 d using the H_2S oxidation protocol, and after pyrite synthesis with and without Co and/or Ni formed using the sulfur oxidation protocol. Reference reflections are shown for mackinawite (red), pyrite (black), elemental sulfur (yellow), greigite (green), and pyrrhotite (blue). Elemental sulfur was a residual phase following the sulfur oxidation protocol.

Figure 2. Phase distribution maps generated from multiple XRF maps within the S K-edge and point XANES in FeS_m synthesized with Co or Ni. For each sample, the end-member XANES points labeled on the map (numbers) correspond to the spectra at right, and their distribution is shown in the same color as the corresponding spectra. Fits are dotted black lines. The fit compositions, as reported in **Table 1,** are also given. Note that FeS_m synthesized without metals was not mapped at multiple XRF energies. A. Results of FeS_m synthesis with Co added. B. Results FeS_m synthesis with Ni added.

Figure 3. Top, S XANES spectra from oxically embedded FeS_m compared to the same sample embedded anoxically (bottom). Data are black circles, and fits are thin black lines.

Figure 4. Phase distribution maps generated from multiple XRF maps within the S K-edge and point XANES in experiments where pyrite was produced from sulfur oxidation. For each sample, the end-member XANES points labeled on the map (numbers) correspond to the spectra at right, and their distribution is shown in the same color as the corresponding spectra. Fits are dotted black lines. The fit compositions, as reported in

Table 1, are also given. A. Results of pyrite synthesis from FeS_m with no metals added. B. Results of pyrite synthesis from FeS_m with Co added. C. Results of pyrite synthesis from FeS_m with Ni added.

Figure 5. Amount of metal in the solids produced from FeS_m and pyrite synthesis in the presence of Co or Ni. The average of triplicate bulk measurements by ICP-AES or ICP-OES are in black, with error bars representing the standard deviation. The median of individual pixels in grains determined on XRF maps collected at 8500 eV. The error bars are standard deviation of these data.

Figure 6. Overplots of endmember FeS_m and pyrite S XANES from samples synthesized with and without Co and Ni. The presence of Ni causes a shift for the pre-edge feature of FeS_m and pyrite to be shifted to higher energy. A subtle shift is observed with Co, but only for FeS_m.

This is a preprint, the final version is subject to change, of the American Mineralogist (MSA)
Cite as Authors (Year) Title. American Mineralogist, in press.
DOI: https://doi.org/10.2138/am-2019-6834

Table 1. Sulfur XANES fit data.

Sample	**Number of Spectra**	**End member (EM) ID**	**FeS**	**Pyrite**	**Poly-sulfide**	**Sulfur**	**Sulfate[a]**	**Comp. Sum**	**chi sq.**
FeS (embedded oxically; 2013)	2	61	0.68				0.37	1.05	6.71
FeS (embedded anoxically; 2014)	10	80	0.68				0.14	0.82	1.29
		88	0.47		0.22		0.21	0.90	1.64
Pyrite (2015)	8	8	0.20	0.74			0.05	0.99	1.33
		10	0.06	0.78			0.11	0.95	0.51
FeS + Co (2015)	7	21	0.80				0.10	0.9	1.78
		25	0.29		0.16		0.32	0.77	1.09
FeS + Co H_2S (2013)	8	23	0.88					0.88	3.13
		24	0.66				0.11	0.77	3.73
Pyrite + Co (2014)	12	4	0.12	0.63	0.22			0.96	1.02
		7			0.29	0.69		0.98	3.17
FeS + Ni (2013)	23	27	0.68				0.14	0.82	1.63
		31	0.62				0.41	1.03	10.01
FeS + Ni H_2S (2013)	10	2	0.82				0.06	0.88	2.84
		4	0.83				0.08	0.91	24.24
Pyrite + Ni (2015)	9	29	0.15	0.73			0.05	0.93	0.69
		35		0.79	0.25			1.04	1.83

[a]The Sulfate standard was quenstedtite.

This is a preprint, the final version is subject to change, of the American Mineralogist (MSA)
Cite as Authors (Year) Title. American Mineralogist, in press.
DOI: https://doi.org/10.2138/am-2019-6834

Table 2. Iron XANES fit data.

Sample	**Number of spectra**	**End member (EM) ID**	**FeS**	**Pyrite**	**Marc-asite**	**Pyrr-hotite**	**Mag-hemite**	**Comp. Sum**	**chi sq.**
Pyrite (2015)	10	15	1.01					1.01	1.55
		16		0.62	0.40			1.02	0.05
		20	0.57	0.43				1.00	2.91
FeS + Co (2013)	8	2	0.70			0.32		1.03	0.49
FeS + Co H_2S (2013)	8	5	1.04					1.04	0.59
Pyrite + Co (2015)	10	53	0.99					0.99	1.20
		54		0.99				0.99	2.16
		58		0.42	0.59			1.01	0.17
FeS + Ni (2015)	8	26	0.70			0.30		1.00	0.24
		30	0.48			0.54		1.02	1.06
FeS + Ni H_2S (2013)	3	1	0.95					0.95	6.85
Pyrite + Ni (2014)	3	43		0.83	0.14			0.97	0.93
		45			0.37		0.51	0.87	9.11

This is a preprint, the final version is subject to change, of the American Mineralogist (MSA)
Cite as Authors (Year) Title. American Mineralogist, in press.
DOI: https://doi.org/10.2138/am-2019-6834

Table 3. Elemental concentrations as determined on digests by ICP-OES or ICP-AES.

Solutions (ppm)			
ICP-OES	**Fe**	**Co**	**Ni**
Ferrous ammonium sulfate (0.6M)	NA	1.36±2.36	4.39±1.37
Hydrogen sulfide (0.6M)	1.67±8.86	BD	BD
Ferrous ammonium sulfate (0.6M) with 2 mM Co	NA	223.20±0.33	4.40±0.84
Ferrous ammonium sulfate (0.6M) with 0.5 mM Ni	NA	1.47±0.41	65.28±0.97
Solids (mg element/g mineral)			
ICP-OES	**Fe**	**Co**	**Ni**
FeS_no_metals	327.53 ±0.23	0.02±0.02	0.05±0.630
FeS_Co	348.56±0.07	3.71±0.06	0.07±0.11
FeS_Ni	319.23±0.36	0.023±0.26	1.05±0.26
FeS_no_metals_20d	480.87±2.60	0.05±6.45	0.06±22.15
FeS_no_metals_4d	483.14±1.65	0.03±10.04	0.027±68.14
FeS_Co_4d	455.96±0.85	4.05±1.92	0.06±2.82
FeS_Ni_4d	493.71±1.13	0.05±0.40	1.43±0.87
ICP-AES	**Fe**	**Co**	**Ni**
Pyrite_no_metals	NA	BD	BD
Pyrite_Co	NA	1.1±0.0	BD
Pyrite_Ni	327.7±20.4	BD	3.4±0.1

NA = element was either not quantified, or element was above the range of quantification.BD=below detection. Detection limits were 0.0008, 0.0011, and 0.0015 ppm for Fe, Co, and Ni, respectively, for ICP-OES. Detection limits were 0.1, 0.1, and 0.2 ppm for Fe, Co, and Ni, respectively for ICP-AES. The relative standard deviations are also reported.

This is a preprint, the final version is subject to change, of the American Mineralogist (MSA)
Cite as Authors (Year) Title. American Mineralogist, in press.
DOI: https://doi.org/10.2138/am-2019-6834

Table 4. Semi-quantitiative Co and Ni concentrations determined from XRF maps.

Solids (mg element/g mineral)	**Element**	**Mean**	**Median**	**e.s.d.**
FeS_Co (2013)	Co	4	3.6	1.6
FeS_Ni (2013)	Ni	0.5	0.4	0.3
FeS_Co_4d (2013)	Co	3.2	3.1	0.7
FeS_Ni_4d (2013)	Ni	0.5	0.4	0.2
Pyrite_Co (2014)	Co	1.6	1.3	0.5
Pyrite_Ni (2014)	Ni	0.6	0.5	0.4

Analytical precision was 0.1 mg element/g FeS_m, which is estimated as the detection limit.

938

This is a preprint, the final version is subject to change, of the American Mineralogist (MSA)
Cite as Authors (Year) Title. American Mineralogist, in press.
DOI: https://doi.org/10.2138/am-2019-6834

Figure 1.

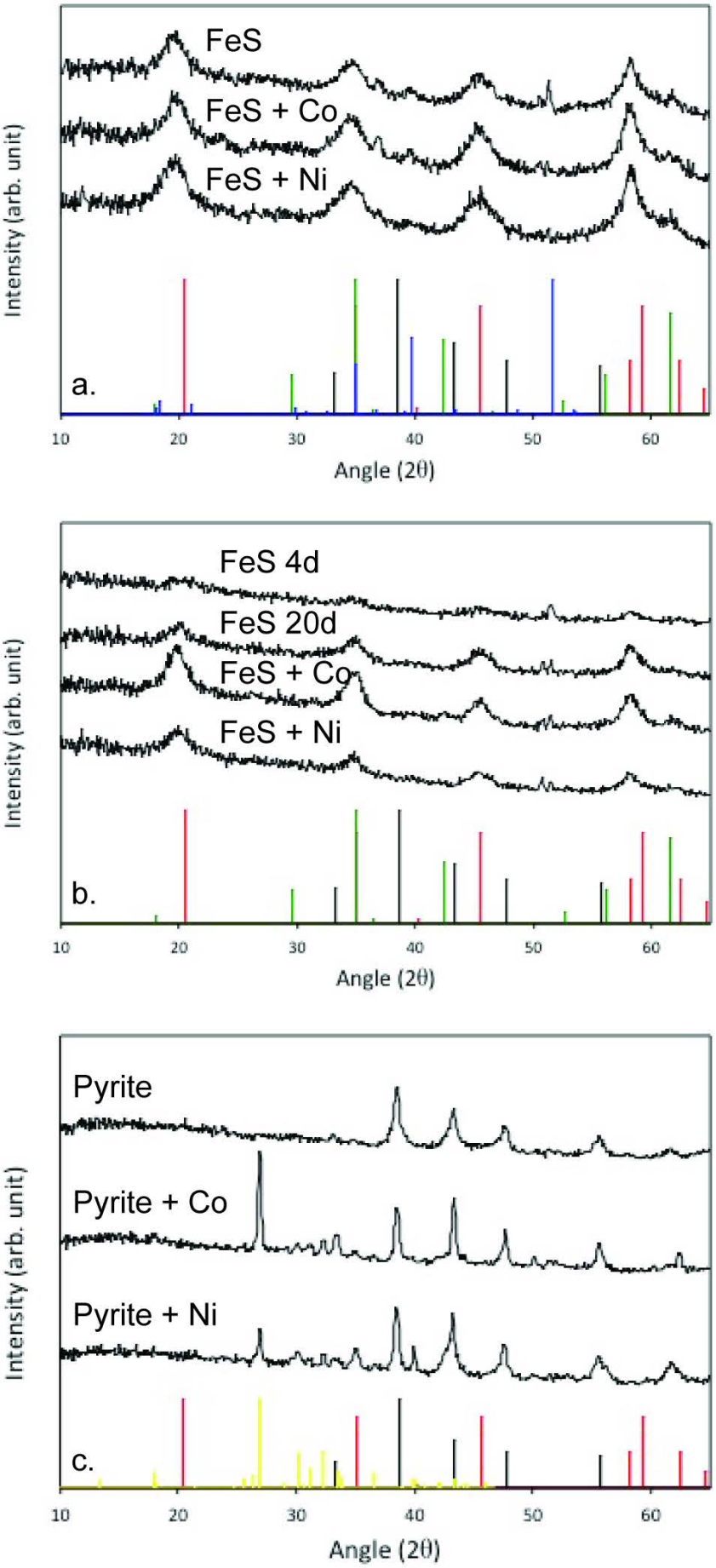

This is a preprint, the final version is subject to change, of the American Mineralogist (MSA)
Cite as Authors (Year) Title. American Mineralogist, in press.
DOI: https://doi.org/10.2138/am-2019-6834

Figure 2

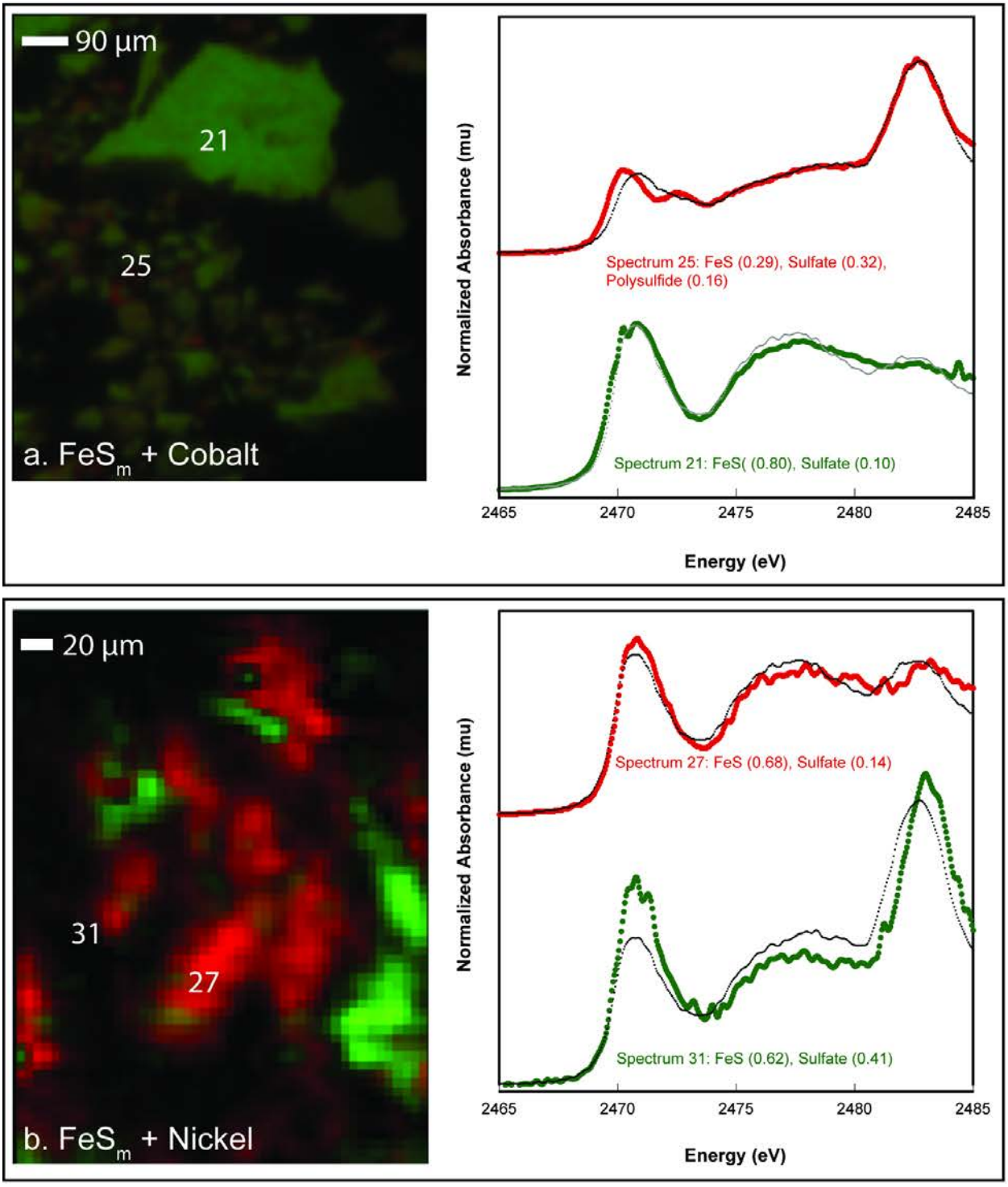

This is a preprint, the final version is subject to change, of the American Mineralogist (MSA)
Cite as Authors (Year) Title. American Mineralogist, in press.
DOI: https://doi.org/10.2138/am-2019-6834

Figure 3.

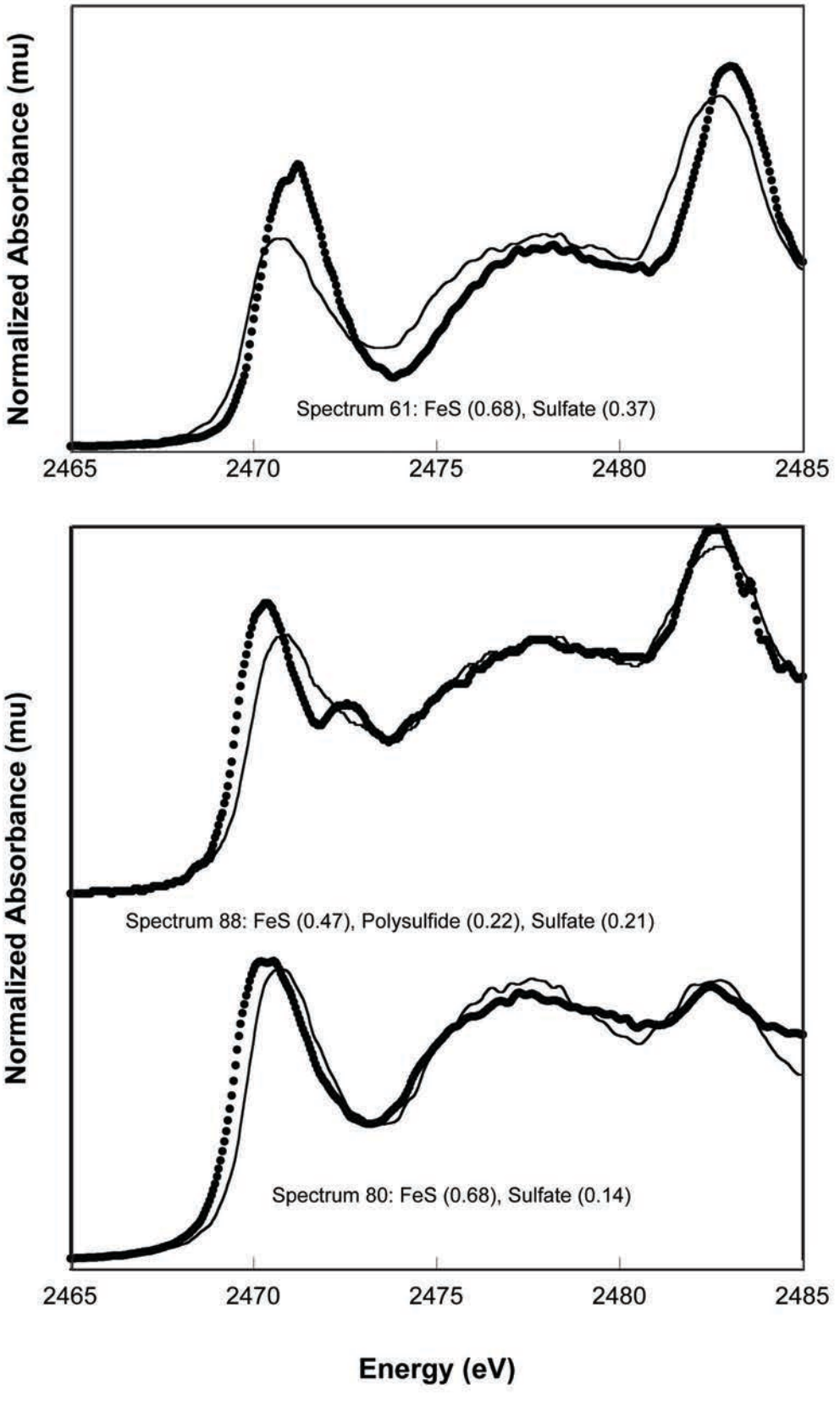

Figure 4.

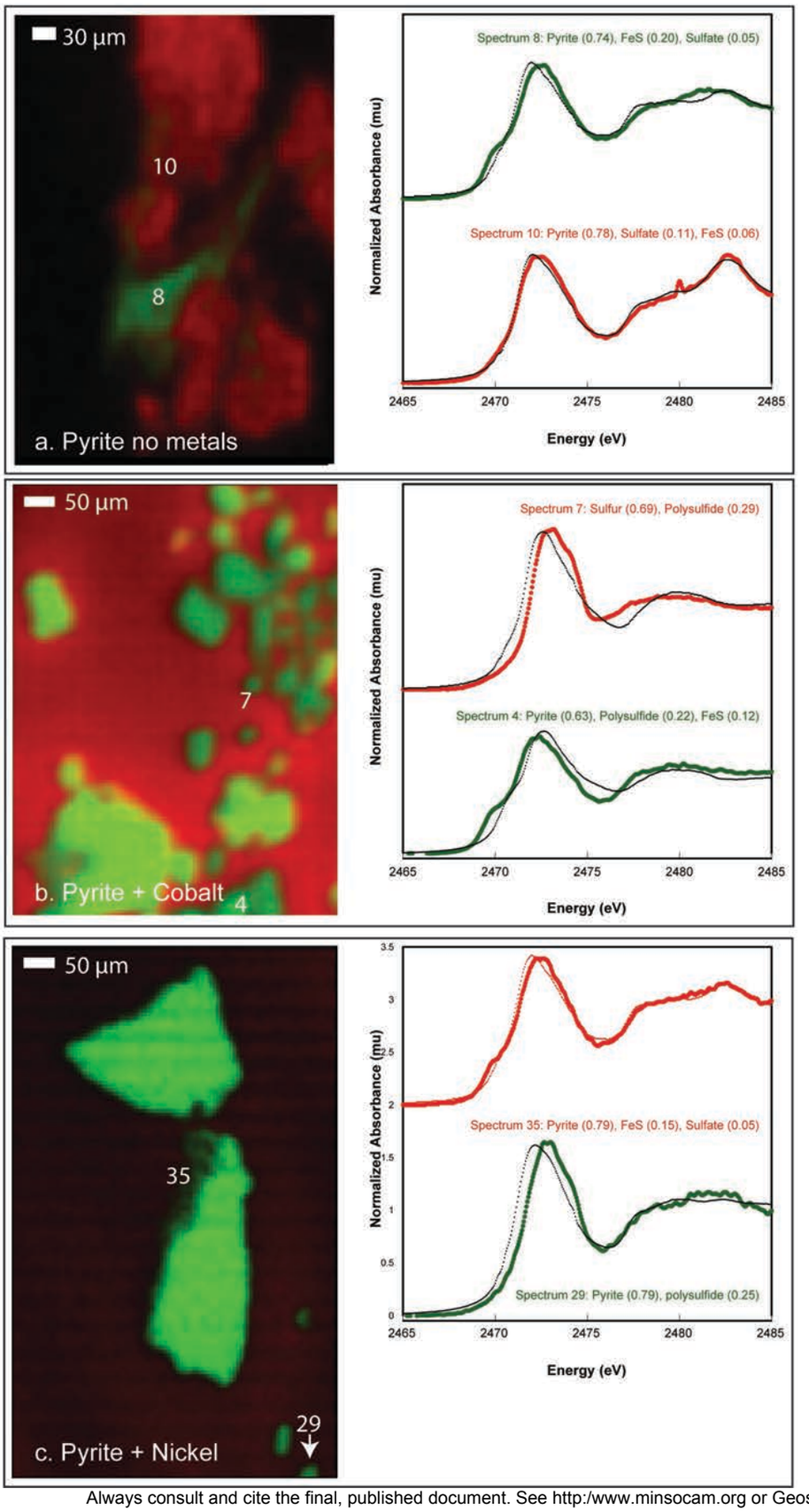

This is a preprint, the final version is subject to change, of the American Mineralogist (MSA)
Cite as Authors (Year) Title. American Mineralogist, in press.
DOI: https://doi.org/10.2138/am-2019-6834

Figure 5.

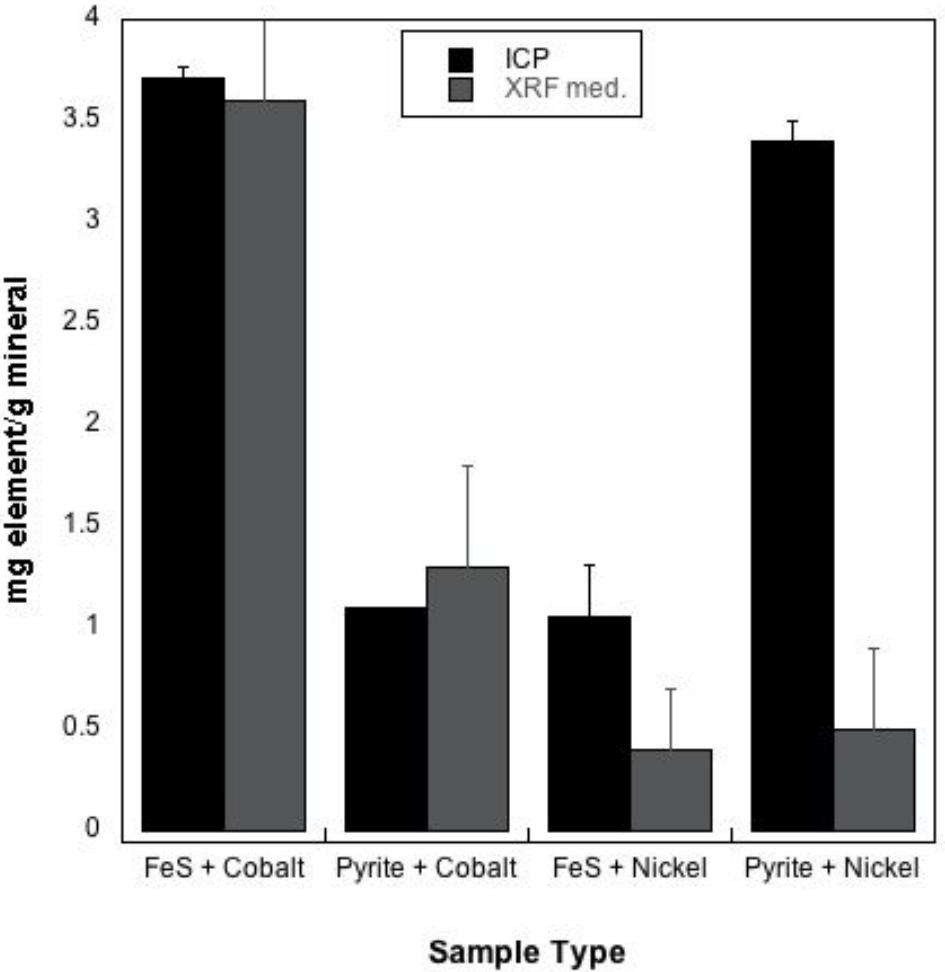

This is a preprint, the final version is subject to change, of the American Mineralogist (MSA)
Cite as Authors (Year) Title. American Mineralogist, in press.
DOI: https://doi.org/10.2138/am-2019-6834

Figure 6.